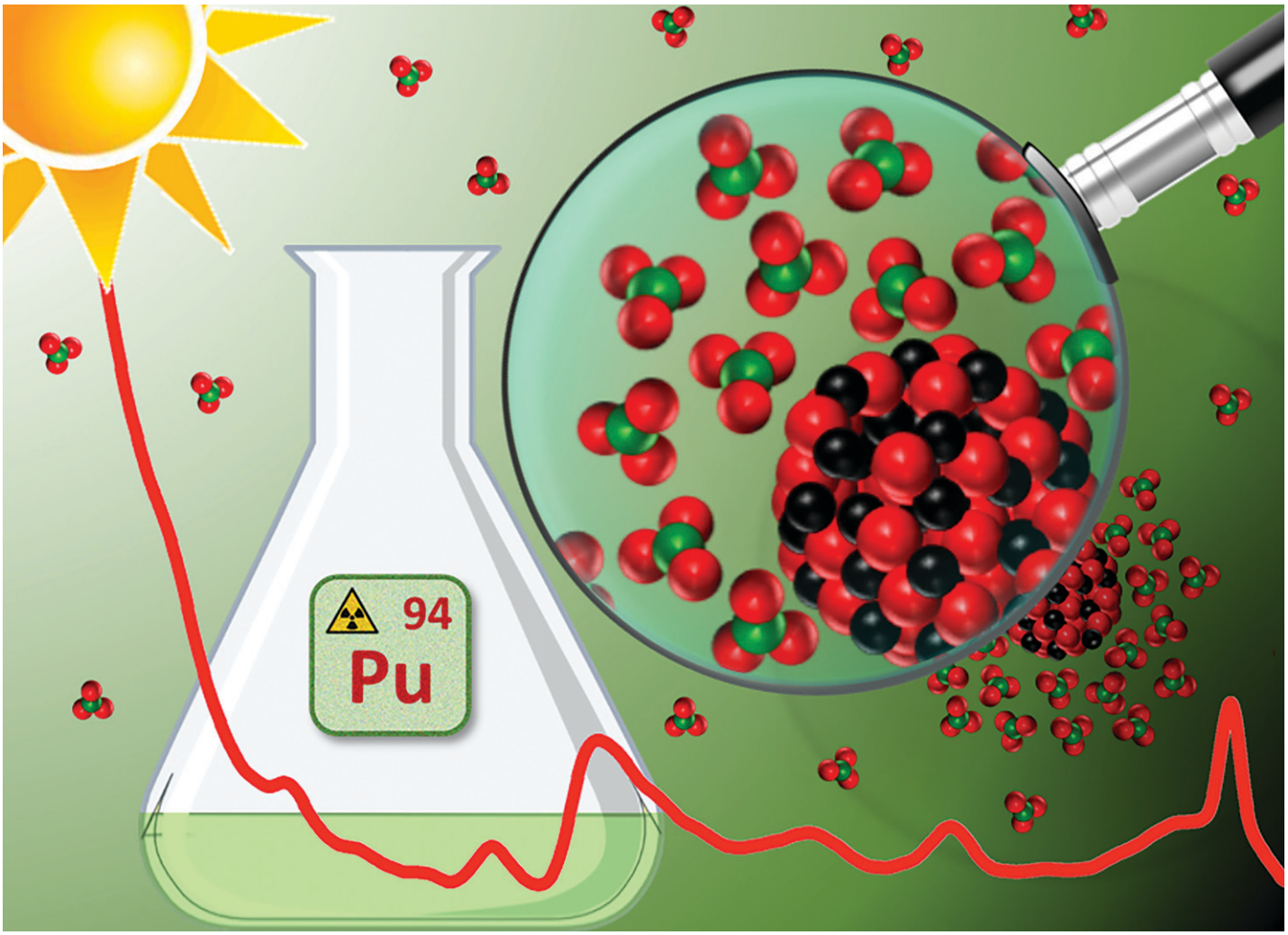


Featuring work from Dr. Matthieu Virot (CEA Researcher) and Dr. Sergey I. Nikitenko (CNRS Research Director) from the Laboratory for Sonochemistry in Complex Fluids (LSFC) at Marcoule Institute for Separation Chemistry (ICSM).

Relevance of formation conditions to the size, morphology and local structure of intrinsic plutonium colloids

Fundamental knowledge of intrinsic plutonium colloids is a key issue in predicting plutonium behaviour in the environment. Combining synchrotron SAXS and XAS (EXAFS/XANES) techniques allows probing the multi-scale structural properties of Pu(IV) intrinsic colloidal suspensions prepared by hydrolysis or sonolysis.

As featured in:



See Matthieu Virot *et al.*, *Environ. Sci.: Nano*, 2020, **7**, 2252.

ROYAL SOCIETY OF CHEMISTRY

rsc.li/es-nano

Registered charity number: 207890

Environmental Science Nano

ROYAL SOCIETY OF CHEMISTRY

PAPER

View Article Online
View Journal | View Issue

Published on 29 June 2020. Downloaded by Los Alamos National Laboratory on 9/3/2025 11:23:41 PM.

Check for updates

Cite this: *Environ. Sci.: Nano*, 2020, 7, 2252

Relevance of formation conditions to the size, morphology and local structure of intrinsic plutonium colloids†

Cyril Micheau,[a] Matthieu Virot, *[a] Sandrine Dourdain, [a] Thomas Dumas, [b] Denis Menut,[c] Pier Lorenzo Solari,[c] Laurent Venault,[b] Olivier Diat, [a] Philippe Moisy [b] and Sergey I. Nikitenko [a]

Received 1st May 2020,
Accepted 28th June 2020

DOI: 10.1039/d0en00457j

rsc.li/es-nano

Fundamental knowledge about plutonium intrinsic colloids is a key issue for the prediction of plutonium transport and release rates in the environment. Recent studies demonstrated that the particle size and surface properties of intrinsic Pu colloids are strongly influenced by the preparation method. In this work, a combination of synchrotron small angle X-ray scattering (SAXS) with X-ray absorption spectroscopy (XAS) is used to characterize two kinds of stable plutonium intrinsic colloids prepared by hydrolysis of Pu(IV) ionic species and sonolysis of PuO_2 in pure water. Despite their similarities, the multi-scale structural properties of these colloidal suspensions are found to be strongly influenced by the synthesis route. The hydrolysis approach leads to spherical nanoparticles of *ca.* 2.0 nm, whereas sonolytic colloids show elongated structures measuring 5.7 nm of thickness and >30 nm long. This difference results from the synthesis mechanism and can be attributed to nanoparticle aggregation in the absence of capping-ions. The results obtained by both SAXS and XAS approaches converge in the description of Pu(IV) intrinsic colloids as core–shell nanoparticles made up of a PuO_2 core covered with a disordered Pu–O shell characterized by a splitting of Pu–O and Pu–Pu distances and an associated strong increase of associated DWF parameters. The local distortions of both Pu–O and Pu–Pu coordination spheres observed by XAS seem to be correlated with the nanoparticle shrinking probed by SAXS rather from the contribution of higher Pu oxidation states. The stabilization of the hydrolytic colloidal particles is further suggested from SAXS simulation to result from interaction with counter-ions from the medium.

Environmental significance

Anthropogenic activities have released considerable amounts of radioactive "hot" particles into the environment. Plutonium element is of significant particular concern due to its migration potential in the colloidal form. Depending on the environmental conditions, the physico-chemical and formation properties of such species can be modified impacting their fate and mobility in the geosphere. Predicting their behaviour and reactivity therefore requires their thorough characterization in their native environment. The combination of synchrotron-based SAXS and XAS experiments described in this study provides new insights regarding Pu(IV) intrinsic colloids which can be described as core–shell nanoparticles whose size, morphology, local structure and interfacial properties are demonstrated to be highly dependent upon the preparation conditions.

Introduction

Anthropogenic activities including nuclear weapon production and testing, disintegration of satellites equipped with nuclear power sources in the atmosphere, or industrial accidents have released substantial amounts of actinides into the environment.[1–4] The element plutonium, which was thought to be highly immobile regarding its very low solubility in aquatic systems and high sorption ability onto minerals, has been proved to move on the scale of kilometers.[1,2,5] Both pseudo- and intrinsic plutonium colloids have been reported to be potentially involved in the environmental migration of actinides, thus strengthening the need for a better description and characterization of their structure.[2,3] Pseudo-colloids usually refer to natural colloids on which Pu has been incorporated or adsorbed, whereas intrinsic ones relies on the ability of Pu to precipitate and form its own colloid. Research progress on Pu(IV) colloids is however particularly challenging because of the complex chemistry of the element Pu and the

[a] *ICSM, UMR 5257, CEA, CNRS, ENSCM, Univ Montpellier, Marcoule, France. E-mail: matthieu.virot@cea.fr*
[b] *CEA, DES, ISEC, DMRC, Univ Montpellier, Marcoule, France*
[c] *Synchrotron SOLEIL, MARS beamline, l'Ormes des Merisiers, Saint Aubin BP 48, 91192 Gif-sur-Yvette, France*

† Electronic supplementary information (ESI) available. See DOI: 10.1039/d0en00457j

This journal is © The Royal Society of Chemistry 2020

Published on 29 June 2020. Downloaded by Los Alamos National Laboratory on 9/3/2025 11:23:41 PM.

high radioactivity of all of its isotopes requiring careful handling.[6] A rigorous characterization of these species is particularly important since the apparent solubility of the colloids strongly depends on the size of the nanoparticles comprising the suspensions.[3,7,8] Furthermore, solubility and interactions with the environment (dissolution, redox interactions, adsorption, complexation, *etc.*) may be significantly impacted by the nanoparticle speciation and the chemical nature of their surface.[9–11]

Tetravalent Pu exhibits an intricate behavior in aqueous solutions due to its tendency to undergo disproportionation and hydrolysis.[6,12–14] The formation of very stable Pu(IV) colloidal suspensions (referred to as intrinsic colloids but also polymers or eigen colloids in the literature) may result through olation or oxolation mechanisms even at relatively high nitric acid concentration (0.5 M).[12,15–17] The preparation of stable suspensions of intrinsic Pu(IV) colloids can be managed through several methods including precipitation from Pu(IV) solutions with alkali and peptization,[6,13] radiolytic processes with Pu ions,[6,18] or "simple" pouring of nitric Pu(IV) solutions at room temperature or boiling pure water.[6,19–21] Recently, an alternative synthesis method using sonochemistry was proposed for the preparation of stable intrinsic Pu(IV) colloids in pure water free of electrolytes or stabilizing agents.[22] The proposed formation mechanism involves the ultrasound-assisted dissolution of bulk PuO_2 powder into Pu(III) ions followed by its reoxidation and subsequent hydrolysis. High resolution transmission electron microscopy (HR-TEM) and X-ray absorption spectroscopy (XAS) techniques allowed these stable colloidal suspensions to be described as quasi-spherical and monodispersed PuO_2-like nanoparticles of *ca.* 7.1 nm in diameter in comparison to the *ca.* 2.9 nm reported for "conventional" hydrolytic colloids.[22] These previous results described both sonochemical and hydrolytic Pu colloids as core–shell nanoparticles composed of PuO_2 cores covered by hydrolyzed Pu(IV) moiety shells.

Despite the growing interest given to intrinsic Pu(IV) colloids in the literature, the physico-chemical properties of these species are still poorly understood. It appears therefore essential to better characterize their structural properties which partly impact their stability and fate under aqueous environmental conditions. The available characterization methods reported so far (LIBD, ALS, XAS, HR-TEM, *etc.*) agree with the description of PuO_2-like nanoparticles or clusters ranging from 1 to several hundreds of nm depending on the synthesis procedure.[6,10,19,20,23] HR-TEM, which appears to be the method of choice for particle size characterization, may nevertheless involve sample alteration during the grid preparation or their measurement (*e.g.* aggregation, oxidation, modification under the beam, drying in the TEM column, *etc.*) that can misrepresent the particle size in colloidal suspensions and suffer from a weak statistics in counting single objects (localized measurements).[24] Alternatively, scattering techniques are very useful to probe directly in the synthesis solution the nanoparticle size and morphology (*i.e.*, shape or form) and the nature of the interactions between the particles without any specific sample preparation. This non-intrusive technique providing *in situ* information averaged over large sample volumes and measurements in the native environment appears therefore ideal for Pu colloidal systems.[24–26]

To our knowledge, only two papers report the use of neutron or X-ray based scattering techniques (SANS and SAXS, respectively) for intrinsic Pu(IV) colloid or nanoparticle characterization.[20,27] Thiyagarajan *et al.* prepared polymeric Pu(IV) colloidal suspensions by diluting and 70 h aging of a 0.09 M Pu(IV) solution in H_2O–HNO_3 (pH = 1.3) followed by 8 h of heating at 95 °C.[20] The related SANS experiments on the absolute scale revealed a highly elongated assembly of Pu oxides, polydispersed in length of more than 190 nm with a diameter of *ca.* 4.7 nm (not observed under electron microscopy). Alternatively, Romanchuk *et al.* precipitated Pu oxide nanoparticles by neutralization of Pu(III), Pu(IV), Pu(V) or Pu(VI) ions with ammonia solutions.[27] HR-TEM investigations pointed at the formation of much more uniform particles (diameter of *ca.* 2.5 nm), whereas SAXS data acquired on these solid samples, on a relative intensity scale, did not provide the accurate determination of the particle size or structure but highlighted a high size polydispersity. The SAXS technique has been recently developed on the MARS beamline of synchrotron SOLEIL (France) which is dedicated to the study of radioactive samples. The high photon flux and high energy combined with the low spectral width of the incident beam allow a better signal definition in a wider Q range in comparison to classical X-ray sources.[25] This analytical bench allows characterization of Pu colloidal suspensions by combining SAXS and XAS measurements. In this work, the simultaneous multi-scale SAXS/XAS characterization of intrinsic Pu(IV) colloids (local structure, size, morphology and aggregation properties) has been carried out using colloidal suspensions prepared by hydrolysis of ionic Pu(IV) in the presence of nitrate ions and sonolysis of PuO_2 powder in pure water.

Experimental

Synthesis of intrinsic Pu(IV) colloids

Plutonium solutions were prepared in a glove box at the Atalante Facility, Marcoule (France). The mother solution of Pu(IV) stabilized in *ca.* 2.5 M HNO_3 was obtained by standard purification onto anion exchange resin.[28] The isotopic composition (wt%) was 96.9% ^{239}Pu, 2.99% ^{240}Pu, 0.06% ^{241}Pu, and 0.02% ^{238}Pu.

A hydrolytic colloidal suspension was obtained by diluting a small volume of Pu(IV) mother solution with Milli-Q water (18.2 MΩ cm at 25 °C) under vigorous stirring (pH 2–3). A green emerald and limpid solution was formed after a few seconds and a steady state was reached after about fifteen days (no more evolution of the UV-vis spectra is observed after this period). The resulting solution had a composition of *ca.* 10 mM Pu and 42 mM HNO_3. This solution was then diluted in 42 mM HNO_3 solution or Milli-Q water to reach

Published on 29 June 2020. Downloaded by Los Alamos National Laboratory on 9/3/2025 11:23:41 PM.

the following plutonium concentrations: 5 mM, 1 mM, 0.5 mM or 0.1 mM.

The sonolytic (or sonochemical) colloidal suspension (pH = *ca.* 3) was synthesized by 20 kHz sonication of PuO_2 nanopowder under an Ar/(10%)CO atmosphere (0.34 W mL^{-1}, 20–21 °C). PuO_2 nanopowder was previously prepared by adding 30 wt% ammonia solution into stirred Pu(IV) acid solutions in the presence of polyethylene glycol (PEG, M = 3000, 2.5 wt%).[29] The precipitates were then heated in air with a constant rate of 10 °C min^{-1} up to 485 °C for 2 h (with a plateau at 120 °C at 1 h). The synthesis of a stable colloidal suspension was carried out by sonicating *ca.* 180 mg of PuO_2 nanopowder dispersed into 50 mL of pure water for 27 h. The obtained mixture was centrifuged (9000 rpm, 2 × 15 min) in order to remove the powder that did not react and isolate the stable colloidal suspension. The detailed study and thorough characterization of these species can be found elsewhere.[22] An aliquot of the obtained green colloidal suspension was diluted 10 times in Milli-Q water. The sonolytic colloid concentration was determined by alpha spectroscopy (Genie 2000, Canberra, France) after deposition and calcination of a 50 μL solution aliquot on an inox disc.

According to previous investigations and the literature, these samples are composed of suspended oxide nanoparticles, supporting the colloidal nature of the aqueous systems under study (IUPAC definition).[2,10,13,22,23,30,31] The above-described synthesis procedures and dilutions allowed stable colloidal suspensions of plutonium, *i.e.* without sedimentation during the duration of the study, to be observed. It is important to emphasize that the sonolytic colloid is nevertheless less stable than the hydrolytic colloid. Flocculation occurs for the former after several months, whereas the latter is stable for several years (samples prepared 5 years ago are still within the form of an optically clear suspension, without sedimentation).

UV-vis absorption spectrophotometry

The UV-vis absorption spectra of the as-prepared intrinsic colloidal suspensions were recorded using a UV3600 Shimadzu spectrophotometer between 350 nm and 1000 nm with 1 cm plastic cuvettes. The measurement cell was placed inside the glove box and connected to the apparatus with optical fibers from outside the enclosure.

Measurement by synchrotron radiation

Small angle X-ray scattering (SAXS) and X-ray absorption spectroscopy (XAS) experiments were performed on the Multi Analyses on Radioactive Samples (MARS) beamline at the synchrotron SOLEIL (Saint-Aubin, France).[32] The storage ring was operating in top-up mode at an electron current of 500 mA, 2.5 GeV. The optics were composed of two long platinum-coated mirrors inserted before and after a double-crystal monochromator (DCM) for beam focusing and specific harmonics rejection. Beam energy calibration was performed at the yttrium edge corresponding to 17.038 keV. The focused beam size on the sample was 300 μm × 400 μm. A specific cell was used for radioactive samples and was composed of Teflon sample holders containing three slots of 250 μL closed by two layers of Kapton® films (polyimide) on each side.

Small angle X-ray scattering (SAXS)

SAXS experiments were carried out with an X-ray energy of 17 keV corresponding to an average wavelength of 0.7294 $Å^{-1}$, and a sample to detector distance of 785.70 mm. This configuration allows a Q-range between about 0.1 nm^{-1} and 18.8 nm^{-1} to be covered. A He gas filled reservoir holding the centered photodiode beam stop was placed between the sample holder and the 2D detector (MAR345) in order to reduce the air scattering. Fig. S1 (ESI†) provides a picture of the analytical bench developed for the combined SAXS/XAS measurements. Sample transmissions were recorded for 10 s using photodiodes and scattering diagrams were recorded for 5 s per sample. Isotropic 2D scattering data were azimuthally averaged to obtain the scattering intensity $I(Q)$ using Fit2D software. The sample scattering intensity was then normalized by the acquisition time, transmission and thickness, and multiplied by a normalization constant determined with the help of the scattering intensity of polyethylene (PE) at Q = 0.36 nm^{-1} that corresponds to 4.9 cm^{-1}. The absolute intensity scattered by colloids was finally obtained by subtracting the empty cell, solvent and background contributions. Data were simulated using the SasView 4.2.0 software (http://www.sasview.org)[33] especially for core–shell, lamella and disk form factors.

Pu L_{III}-edge X-ray absorption spectroscopy (XAS)

Experimental spectra were recorded in fluorescence mode using a Ge multi-element detector at the Pu L_{III}-edge (see Fig. S1, ESI†). The samples were oriented at 45° with respect to the incident beam. The incident energy was calibrated using a metallic Zr foil (K-edge defined at 17.988 keV). Pu ionization energy was defined at the maximum of the white line and corresponds to 18.068 keV. Each XAS spectrum corresponds to the average of 3 to 7 pre-processing scans obtained after *ca.* 60 to 90 min of analysis. XANES spectra were extracted by subtraction of the pre-edge background absorption and normalization of the edge to an absorbance value of 1. EXAFS data were analyzed with Athena and Arthemis software from the IFEFFIT package.[34] Fits were obtained using a Kaiser–Bessel window in the 2.5 $Å^{-1} < k <$ 15 $Å^{-1}$ range of the k^3-weighted spectra (FEFF8.4 program).[35]

To avoid misinterpretations, the data treatment was standardized. A second fitting approach was compared by treating the first Pu–O shell separately to avoid artefact generation from the long k range in agreement with a previous report.[36] Briefly, the normalization, background subtraction and Fourier transform (FT) of the Pu–O shell were performed on the normalized absorption spectra truncated at k = 10 $Å^{-1}$ to avoid interferences with the Pu–Pu coordination sphere. A back FT was then carried out in the R–φ = 1.1–2.5 Å range and a

 This journal is © The Royal Society of Chemistry 2020

Published on 29 June 2020. Downloaded by Los Alamos National Laboratory on 9/3/2025 11:23:41 PM.

single Pu–O path was used to fit the back-Fourier transform. The Debye–Waller factor (DWF, σ^2) was considered as a floating parameter, while the coordination number (CN) and the Pu–O distance parameters were fixed to 8 and 2.34 Å, respectively, in agreement with the ideal PuO_2 fluorite structure. The Pu–Pu shell was treated on the FT of the k^3-weighted EXAFS in the 2.5–15 $Å^{-1}$ range where the DWF, R_{Pu-Pu} and CN were considered as floating parameters.

Experimental spectra of bulk PuO_2 powder obtained by thermal conversion of Pu(IV) oxalate at 650 °C were used as a reference. In addition, the theoretical EXAFS spectrum of the Pu38 cluster published by Soderholm *et al.*[12] was generated for comparison by preserving all of the atomic positions with the exception of the 54 chlorine atoms at the particle surface that were substituted by 24 μ_1-OH groups, 24 μ_2-OH groups and 6 H_2O molecules at 2.25 Å, 2.32 Å and 2.50 Å, respectively. The DWF parameters were fixed according to available EXAFS measurements on actinide hexanuclear clusters (0.003 $Å^2$ for μ_1-OH and μ_3-O bonds; 0.005 $Å^2$ for μ_4-O, H_2O molecules and Pu–Pu interactions).[37,38] The EXAFS oscillations calculated for the 38 Pu atoms are then averaged to produce the spectrum.

Results and discussion

Synthesis and absorption spectroscopy

Hydrolytic and sonolytic Pu(IV) intrinsic colloids, respectively, were prepared by dilution of a Pu(IV) solution stabilized in nitric acid with pure water and by extended sonication (20 kHz ultrasound, Ar/(10%)CO, 20 ± 1 °C) of bulk PuO_2 powder dispersed in pure water (see details in the ESI†).[22] Whatever the synthesis procedure, stable (*i.e.*, without sedimentation), limpid and green colloidal suspensions were obtained. The UV-vis absorption spectra of both hydrolytic and sonolytic colloidal suspensions are provided in Fig. 1. The hydrolytic colloid spectrum displays four peaks located at λ = 578 nm, 615 nm, 688 nm and 735 nm, characteristic of intrinsic Pu(IV) colloids.[6,22,31,39,40] The high absorption region observed for λ < 550 nm can be attributed to Mie scattering, in agreement with the presence of suspended nanoparticles in this sample. These features agree with the sonolytic colloid spectrum with however a lower intensity for the absorption bands which evidence a lower nanoparticle concentration for this sample. The sharp peak located at 830 nm is only observed for the hydrolytic colloid spectrum, indicating the presence of Pu(VI) ion traces in the solution.[22] This species results from Pu(IV) disproportionation (eqn (1)) and chemical oxidation of Pu(V) by Pu(IV) in weakly acidic solution (eqn (2)), and corresponds to a Pu concentration lower than 0.32 mM (<3.2%, with ε_{830} = 555 M^{-1} cm^{-1}).[6,41] Both eqn (1) (slow step) and eqn (2) (rapid equilibrium) can be summarized by eqn (3). Note that Pu(IV) disproportionation depends on the H^+ concentration at the fourth order and is therefore not favored at high acidity.[6] The absence of Pu(III) under these conditions may be explained by the catalytic oxidation of Pu(III) according to eqn (4) and (5), but also by the low molar extinction coefficient of Pu(III).

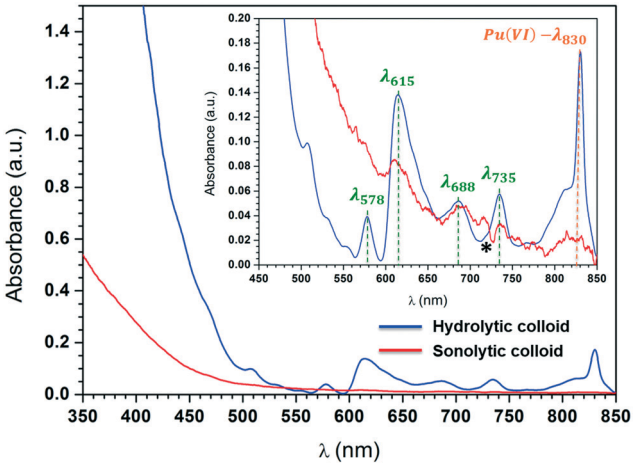


Fig. 1 UV-vis absorption spectra of 10 mM hydrolytic (blue line) and 0.8 mM sonolytic (red line) intrinsic colloids. Characteristic bands are indicated in the inset with dotted lines (λ = 578, 615, 688 and 735 nm) where the intensity of the sonolytic colloid is multiplied by 7 and the black star (*) indicates an artefact due to the optical fibers. The Pu(VI) absorption band located at λ = 830 nm is indicated in orange. Despite this high absorption band, the concentration of Pu(VI) in the solution is less than 3.2% of the total Pu concentration.

$$2Pu^{4+} + 2H_2O \rightleftarrows Pu^{3+} + PuO_2^{+} + 4H^{+} \quad (1)$$

$$Pu^{4+} + PuO_2^{+} \rightleftarrows Pu^{3+} + PuO_2^{2+} \quad (2)$$

$$3Pu^{4+} + 2H_2O \rightleftarrows 2Pu^{3+} + PuO_2^{2+} + 4H^{+} \quad (3)$$

$$2Pu^{3+} + 3H^{+} + NO_3^{-} \rightarrow 2Pu^{4+} + HNO_2 + H_2O \quad (4)$$

$$Pu^{3+} + HNO_2 + H^{+} \rightarrow Pu^{4+} + NO + H_2O \quad (5)$$

Dilution of the as-prepared hydrolytic colloidal suspensions in 42 mM HNO_3 or pure water preserves the optically clear solutions (*i.e.*, without sedimentation) and does not modify the position of the absorption signals (the intensity decrease is related to the lower concentration of the colloids in the suspensions), as evidenced by the spectra provided in the ESI† (see Fig. S2, S3 and S4). The list of the mother and dilute samples (and related composition) is gathered in Table 1. By assuming total Pu(IV) conversion into a Pu(IV) colloid, the molar absorption coefficient of the hydrolytic colloid suspension at λ = 615 nm is approximated to be about 13 M^{-1} cm^{-1}. This value suffers from reliability due to the absence of comparison data in the literature attributed to uncertainties and a lack of reproducibility concerning nanoparticle sizes and concentrations.[39,40]

SAXS analysis: characterization of the particle size, morphology and aggregation properties

The normalized SAXS diagrams measured for the mother solutions of both hydrolytic and sonolytic colloids (denoted as HC-10-HNO_3 and SC-0.8-H_2O respectively, in Table 1) are given in absolute units in Fig. 2. A different scattering pattern

Published on 29 June 2020. Downloaded by Los Alamos National Laboratory on 9/3/2025 11:23:41 PM.

Table 1 Hydrolytic (HC) and sonolytic (SC) colloidal suspension compositions, theoretical volume fraction (ϕ_{th}) calculated for total Pu(IV) conversion into a colloid and based on the PuO_2 molar volume, and core volume fraction (ϕ_{core}) determined from the I_0 value of the core–shell fitting model. All of the as-prepared solutions were stable and optically clear without sedimentation during the whole experiment

Sample name	[Pu]/[HNO_3]	ϕ_{th} (%)	ϕ_{core}[a] (%)
Hydrolytic colloid (HC)			
HC-10-HNO_3	10 mM/42 mM	0.024	0.017
HC-5-HNO_3	5 mM/42 mM	0.012	0.008
HC-1-HNO_3	1 mM/42 mM	0.0024	—
HC-0.5-HNO_3	0.5 mM/42 mM	0.0012	0.0003
HC-0.1-HNO_3	0.1 mM/42 mM	0.00024	—
HC-5-H_2O	5 mM/21 mM	0.012	0.008
HC-1-H_2O	1 mM/11 mM	0.0024	0.0011
Sonolytic colloid (SC)			
SC-0.8-H_2O	0.8 mM/0 mM	—	—
SC-0.08-H_2O	0.08 mM/0 mM	—	—

[a] Calculated from core–shell simulation.

underlining strong differences in particle size and morphology for both kinds of samples is clearly observed. To our knowledge, this is the first time that SAXS diagrams in absolute unit are reported for stable Pu colloidal suspensions in such a wide Q-range. This configuration is of high potential for data fitting and initial intensity (I_0) analysis. The slope displayed for the hydrolytic colloid is Q^0 for low wave vectors and tends towards Q^{-4} at higher wave vectors, which is characteristic of a sharp interface, typical for three-dimensional objects and compact particles.[25,42,43] The slope of the scattering curve of the sonolytic colloid exhibits a closer Q^{-2} at low wave vectors, which ends with a Q^{-4} at larger wave vectors. These features are often attributed to two-dimensional elongated objects such as infinitely thin disks or lamellas.[25]

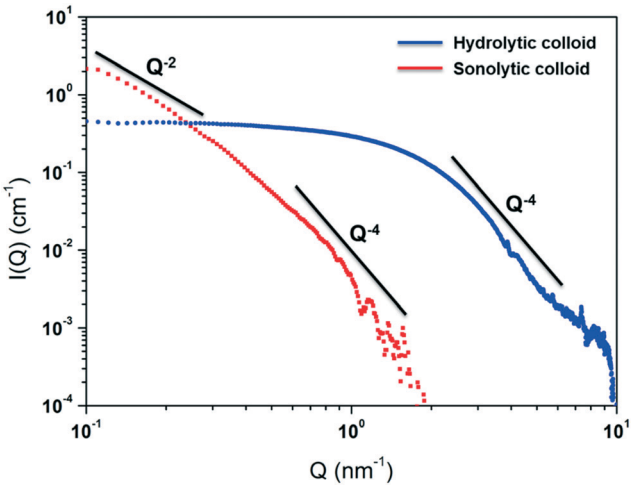


Fig. 2 SAXS diagrams of 10 mM hydrolytic (blue line) and 0.8 mM sonolytic (red line) intrinsic Pu(IV) colloids. Black lines indicate the slope power laws. The oscillation at Q = 4 nm^{-1} is an artefact attributed to the scattering of the Kapton windows of the sample holder.

In the present work, the large wave vector reached for the stable colloidal suspensions allows the determination of the particle sizes with a good approximation using simple fitting models. SAXS scattering diagrams are generally described with the following equation (eqn (6)) where I_0 is the initial intensity for Q approaching 0 value (very small angles), $P(Q)$ is the form factor which provides information about the particle size and morphology, and $S(Q)$ is the structure factor which provides information about the interactions between the particles. This last function equals unity for dilute solutions.

$$I(Q) = I_0 P(Q) S(Q) \quad (6)$$

Table 2 summarizes the molar volume V_m, the scattering length density ρ_c and the contrast $\Delta\rho^2$ used for the calculations. The high electron density of plutonium offers a very high contrast with the bulk solution (the scattering length density of 42 mM nitric acid solution does not differ significantly from that of pure water: 9.434 × 10^{10} cm^{-2} against 9.428 × 10^{10} cm^{-2}, respectively). SAXS diagrams obtained for the sonolytic colloid do not reach the Q^0 plateau at low wave vectors. Moreover, the Porod law in a high Q range cannot be observed due to the low colloidal concentration. These two assertions explain the difficulty in determining the $S(Q)$ contribution in eqn (6). However, due to the low colloid concentration, it was assumed that $S(Q)$ = 1. The fit results are provided in Table 3 and the corresponding simulated curves are compared to the experimental ones in Fig. 3a for infinitely thin lamella and disk models. Fit models result in a limit size value of 3.77(50) nm in thickness in the lamella model and about 5.29(50) nm in thickness and 15.98 nm as a minimum radius in the case of the disk model (see Table 3). A better reproducibility is observed with the disk model when comparing the sonolytic colloid (SC-0.8-H_2O) and its dilute sample (SC-0.08-H_2O: L = 6.13 nm and $R_D > 15.81$ nm; see Fig. S5, ESI†).

To evaluate a possible $S(Q)$ factor for the hydrolytic colloid, the mother solution of the 10 mM hydrolytic colloid (HC-10-HNO_3) was diluted in 42 mM HNO_3 solution or pure water (see Table 1). The corresponding SAXS diagrams, normalized by their theoretical volume fraction (ϕ_{th}), are plotted in Fig. S6, ESI† (HC-0.1-HNO_3 sample diagram was not usable due to the too low particle concentration of the suspension that did not scatter enough). All the curves are overlapping, which indicates the absence of significant interactions between the nanoparticles comprising the various Pu suspensions in the concentration range studied (10–0.5 mM). In addition, it is very important to emphasize

Table 2 Molar volume (V_m), X-ray scattering length density (ρ_c) and electron contrast ($\Delta\rho^2$) used for SAXS diagram simulation calculations. Values for PuO_2 are based on the dense oxide density (d = 11.5)

	V_m (10^{-23} cm^3)	ρ_c (10^{10} cm^{-2})		$\Delta\rho^2$ (10^{23} cm^{-4})
PuO_2	3.99	77.78	PuO_2/H_2O	4.672
H_2O	2.99	9.43		

This journal is © The Royal Society of Chemistry 2020

Published on 29 June 2020. Downloaded by Los Alamos National Laboratory on 9/3/2025 11:23:41 PM.

Table 3 Simulation results of SAXS diagrams obtained with SasView software: I_0 is the intensity for $Q \rightarrow 0$, R_G the gyration radius, R the radius of the sphere, R_{core} the radius of the core, T_{shell} the thickness of the shell, ρ_{shell} the scattering length density of the shell, L the thickness of the lamellar or disk and R_D the radius of the disk. The standard deviation of the variable parameters estimated using SasView is indicated in brackets

Sample information		Model								
		Guinier		Sphere	Core–shell			Lamella	Disk	
Name	I_0 (cm^{-1})	R_G (nm)	R (nm)	R (nm)	R_{core} (nm)	T_{shell} (nm)	ρ_{shell} (10^{10} cm^{-2})	L (nm)	L (nm)	R_D (nm)
Hydrolytic colloid (HC)										
HC-10-HNO_3	0.42(2)	1.04(5)	1.34(7)	1.30(10)	0.93(10)	1.45(20)	10.64(50)	—	—	—
HC-5-HNO_3	0.20(2)	1.01(5)	1.304(70)	1.25(10)	0.95(10)	1.25(20)	10.93(50)	—	—	—
HC-0.5-HNO_3	0.013(5)	1.01(5)	1.304(70)	1.23(10)	1.23(10)	—[a]	13.51(50)	—	—	—
HC-5-H_2O	0.20(8)	1.01(5)	1.304(70)	1.25(10)	0.90(10)	1.03(20)	11.91(50)	—	—	—
HC-1-H_2O	0.036(20)	1.01(2)	1.30(3)	1.27(10)	1.08(10)	1.56(20)	10.36(50)	—	—	—
Sonolytic colloid (SC)										
SC-0.8-H_2O	2.2(5)	—	—	—	—	—	—	3.77(50)	5.29(50)	>15.98(10)
SC-0.08-H_2O	0.06(1)	—	—	—	—	—	—	—[b]	6.13(60)	>15.81(10)

[a] Not discernable by SasView – high dilution limits the data statistics in a high Q range. [b] Model does not fit.

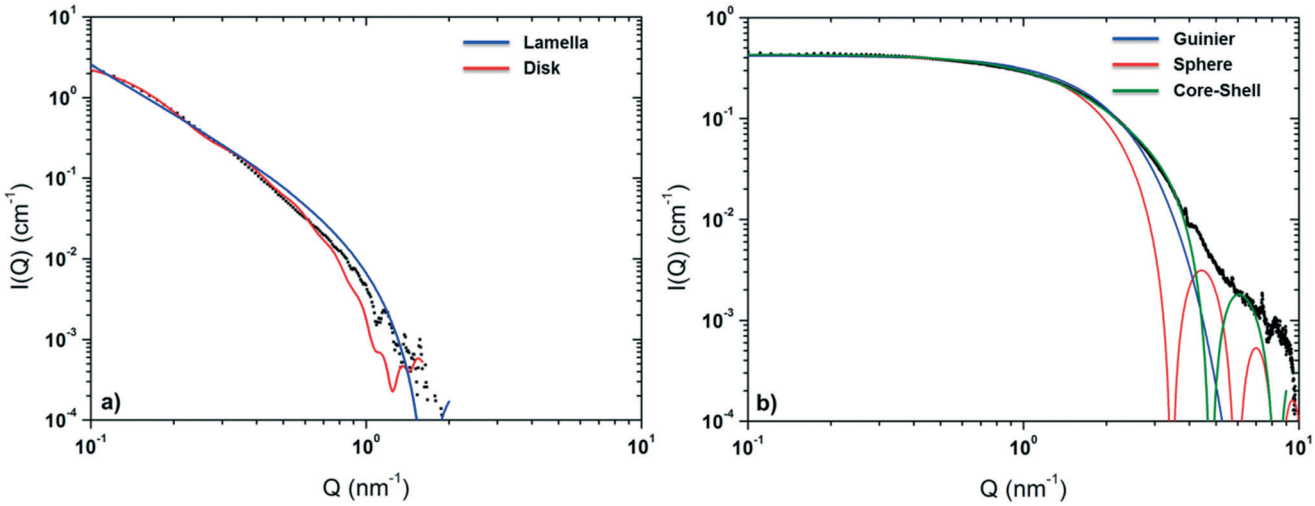


Fig. 3 Fit models applied to: a) 0.8 mM sonolytic colloid (SC-0.8-H_2O) diagram: lamella model (blue line) and disk model (red line), and b) 10 mM hydrolytic colloid (HC-10-HNO_3) SAXS diagram: Guinier model (black line), sphere form factor (red line) and spherical core–shell form factor (green line).

that the similarity between the scattering diagrams of the various hydrolytic colloids diluted in HNO_3 or H_2O (Fig. S6, ESI†) also indicates a poor ionic strength effect on the particle size and morphology (*i.e.*, shape). These observations allow the $S(Q)$ parameter to be considered equal to 1 for all of the hydrolytic colloid samples in the equation (eqn (6)).

Hydrolytic colloid diagrams were then fitted using three different models (see the ESI† for model descriptions):[42,44,45] (i) Guinier model, (ii) monodisperse sphere form factor model, and (iii) spherical core–shell model (Fig. 3b). In the first two models, the initial intensity is defined with the equation described hereinafter (eqn (7)) with ϕ_P, the volume fraction of the particle, V_P, its volume and $\Delta\rho^2$, the electronic contrast with the solvent.[44]

$$I_0 = \varphi_P V_P \Delta\rho^2 \quad (7)$$

(i) Guinier analysis, which gives a first approach of the particle radius of gyration R_G by fitting the Q^0 plateau and the inflexion of the SAXS curve, fails however by fitting the data for $Q > 3$ nm^{-1}. A radius of gyration of *ca.* 1 nm is found for all of the hydrolytic colloid samples (see Table 3). The radius of gyration is known to be greatly affected by particle shape, aggregation, unsuitable solvent, background subtraction and polydispersity.[42] Considering spherical and filled particles, the radius of the particles can be deduced with the following equation (eqn (8)) where R is the radius of the sphere.

$$R_G = R\sqrt{(3/5)} \quad (8)$$

The determined radius of 1.3 nm (see Table 3) is in good agreement with the literature data discussing the nanoparticle size comprising intrinsic Pu(IV) colloidal suspensions.[10,19,22,23] (ii) The best fits obtained with the monodisperse sphere form factor model are also consistent with a sphere radius R of about 1.3 nm agreeing with the Guinier model (red line, Fig. 3b and Table 3). Gaussian and lognormal polydispersities

Published on 29 June 2020. Downloaded by Los Alamos National Laboratory on 9/3/2025 11:23:41 PM.

were tentatively applied to improve the model, particularly for data $Q > 1.5$ nm^{-1}, however without significant improvement (see Fig. S5, ESI†). Extending this model to the four other hydrolytic colloid samples leads to the same particle size strengthening the absence of influence of the media on the size and morphology (*i.e.*, the shape) of the hydrolytic colloid mother solution (HC-10-HNO_3) and its dilute samples.

(iii) The spherical core–shell model involves fitting the nanoparticle spherical core radius R_{core}, the shell thickness T_{shell}, the scattering length density of the shell ρ_{shell} and the volume fraction of the colloid. For simplicity, the colloid core was assumed to have an ideal PuO_2 fluorite-type $Fm\bar{3}m$ oxide structure with a scattering length density defined in Table 2. The fits performed on the five hydrolytic colloid scattering diagrams were found to converge to similar values with $0.90 < R_{core} < 1.08$ nm and $1.03 < T_{shell} < 1.45$ nm with an average $\rho_{shell} = 10.96 \times 10^{10}$ cm^{-2}. The HC-0.5-HNO_3 sample is different from the others because only a core radius could be fit. This is likely due to the poor statistics data in the high Q range for this highly diluted sample. Furthermore, the volume fraction of the core extracted from the fitted I_0 values of each sample is found to be slightly lower but consistent with the theoretical volume fraction given in Table 1. Such observations underline the good reproducibility of the fitting procedure and strengthen the relevance of this core–shell model.

These results raise the question of the origin and nature of the shell that surrounds the PuO_2 nanoparticle core in nitric acid solutions. The scattering length density values obtained with the simulation are slightly higher than those of pure water, indicating an excess of electron density surrounding the nanoparticle surface. Such an excess can be induced by the presence of Pu–OH surface functions, μ_3-oxo bonds, nanoparticle curvature, surface roughness, *etc.*[22,46,47] Nevertheless, these parameters only account for the rising electronic density but do not explain the thickness and composition of this shell in the presence of H^+ and NO_3^- ions. According to the core–shell model, this shell corresponds to several atomic layers (*ca.* 1.32 nm). Abdel-Fattah *et al.* have previously performed zeta potential measurements on PuO_2 particles of around 100 nm size.[48] Their results showed that PuO_2 particles are positively charged for pH values lower than the isoelectric point (8.6) and correspond to a zeta potential of *ca.* 60 mV for pH < 3.

This positive charge is the surface charge of the Stern–Helmholtz layer which corresponds to the stationary hydration layer and the attached counter-ion layer. The whole is surrounded by the diffuse layer (or Gouy–Chapman layer) which contains mobile co-ions and counter ions. Both layers (Gouy–Chapman and Stern), in addition to other possible functions existing at the particle surface (*i.e.*, hydroxo and oxo groups, adsorbed water, *etc.*), may contribute to the scattering length density of the shell in the current model. Yet, it remains difficult to distinguish between them. By considering only nitrate NO_3^- as a counter-ion with an ionic radius of *ca.* 200 pm,[49] a shell composed of *ca.* 3.3 compact layers of NO_3^- can be deduced which corresponds to a local concentration of *ca.* 3.6 M (Fig. 4). An attempt to improve this fitting model was made using a scattering length density gradient profile (Fig. S5, ESI†) but this model remains less satisfactory than the core–shell model. Alternative models such as a multilayer model (*i.e.* onion-like form factor) could be used to improve the fitting method with higher statistics in the high Q range which might be obtained with more concentrated solutions. Considering this first dataset, the core–shell model gives nevertheless a consistent explanation for the intrinsic Pu(IV) hydrolytic colloid morphology (shape).

The size of the core (around 2.0(3) nm in diameter) determined for the hydrolytic colloids agrees with previous HR-TEM observations performed on such nanoparticles.[10,19,22,23] By contrast, previous HR-TEM investigations carried out on intrinsic sonolytic colloids revealed the presence of quasi-spherical particles with an average diameter of about 7.1 nm (see pictures in Fig. S7, ESI†).[22] The particle size discrepancies noticed when comparing previous microscopy results with the current SAXS values could arise from three different factors: (i) the HR-TEM sample preparation involves a drying step,[24] (ii) the different PuO_2 precursors used during sonolysis in the two studies (nanostructured PuO_2 composed of *ca.* 10 nm sintered particles *vs.* a nanopowder composed of *ca.* 5 nm particles in the current study)[22] and (iii) a possible aggregation or flocculation phenomenon occurring with the nanoparticles in the colloidal suspension, even after dilution in water. This last hypothesis observation also agrees with the lower stability observed for the sonolytic colloid (several months) in comparison to the hydrolytic colloid (>several years).

Furthermore, this aggregation phenomenon was already mentioned by Thiyagarajan *et al.* who performed SANS characterization on intrinsic Pu(IV) colloidal suspensions.[20] These stable colloids, prepared by the heating method, were found to be composed of aggregated and ellipsoidal

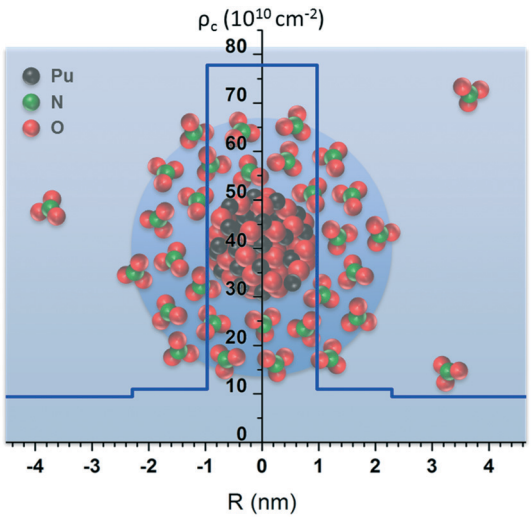


Fig. 4 X-Ray scattering length density profile of the intrinsic Pu(IV) hydrolytic colloid and representation of the spherical colloid composed of a PuO_2 core surrounded by a shell containing nitrate ions in bulk solution drawn from SasView simulation results.

 This journal is © The Royal Society of Chemistry 2020

Published on 29 June 2020. Downloaded by Los Alamos National Laboratory on 9/3/2025 11:23:41 PM.

nanoparticles of *ca.* 4.7 nm in diameter and more than 190 nm long.[6,20] A Q^{-2} slope has also been observed by Romanchuk *et al.* on SAXS diagrams obtained from precipitated PuO_2 nanoparticles of *ca.* 2.5 nm diameter in agreement with their HR-TEM data.[27] In this case, the precise shape of the precipitated PuO_2 nanoparticles was not determined with SAXS. Some possible particle agglomeration was proposed to explain the Q^{-2} decay observed in the scattering diagrams.[27] Whatever the study, determining the longest dimension of such elongated particles is technically difficult because of the low Q-range accessibility (limited sample–detector distance). In any case, the observation of these elongated or agglomerated nanoparticles raises the question of the charge and surface nature of these particles.

SAXS results point out that comparable sonolytic and hydrolytic intrinsic Pu(IV) colloids may display a different pattern that corresponds to an elongated slab and spherical core–shell, respectively. This difference may be attributed to the synthesis method itself and the related formation mechanism of the nanoparticles. While the hydrolytic intrinsic Pu(IV) colloid is formed by hydrolysis of Pu^{4+} ions (in competition with disproportionation), the sonolytic intrinsic Pu(IV) colloid has been proposed to be formed in a two-step process: (i) reductive dissolution of the bulk PuO_2 nanopowder accumulating Pu(III) in solution, followed by (ii) reoxidation and hydrolysis of Pu(IV).[22] In addition, the contrasted particle shape may also arise from the difference in the solvent nature during synthesis: pure water (salt free) *vs.* nitrate solution. In the case of the hydrolytic colloid, the presence of the electrolyte induces the formation of a counter-ion layer (coordinated or not) at the particle surface that may prevent agglomeration. Further investigations, especially on the nanoparticle surface charge, need to be performed to elucidate this phenomenon.

XAS analysis: local structure and nanoscale effects

The Pu L_{III} edge X-ray absorption near-edge structure (XANES) spectra acquired for a selection of hydrolytic and sonolytic colloid samples (HC-10-HNO_3, HC-5-HNO_3, HC-5-H_2O and SC-0.8-H_2O) are presented in Fig. 5a and S8 (ESI†). Pu L_{III} XANES allows the unoccupied Pu 6d states to be investigated and is a good tool for probing the oxidation state. The synchrotron measurements of the colloidal suspensions performed over at least 4 hours did not show any significant variation as emphasized with the spectra provided in Fig. S9, ESI.† This important point combined with the absence of sedimentation and with the long term stability of the colloidal suspensions (checked with absorption spectroscopy) validates our result and demonstrates the absence of significant redox transformations or beam damage during our study. Good spectra similarities in terms of shape, position and intensities can indeed be observed between the studied colloidal samples and also with bulk PuO_2 powder used for comparison in Fig. 5a (derivatives are given in Fig. S10, ESI†). This observation also agrees with XANES spectra of Pu(IV) intrinsic colloids from the literature.[15,22,50,51] The energy position of the white line (WL) evidences a similar electronic structure (<1 eV difference) for all of the samples: 18 068.4 eV for SC-0.8-H_2O, 18 068.0 eV for the PuO_2 reference and 18 067.4 eV for all of the hydrolytic colloids (HC-10-HNO_3, HC-5-HNO_3 and HC-5-H_2O).

In comparison to molecular Pu(IV),[47,49] plutonium intrinsic colloids show a similar position with a lower amplitude combined with a wider and asymmetrical WL, as recently evidenced by Vitova *et al.*[50] In this study, the authors combined XANES and computations to demonstrate that intrinsic Pu(IV) colloids exhibit band-like 6d states similar to bulk PuO_2, contrasting with the narrower 6d states expected

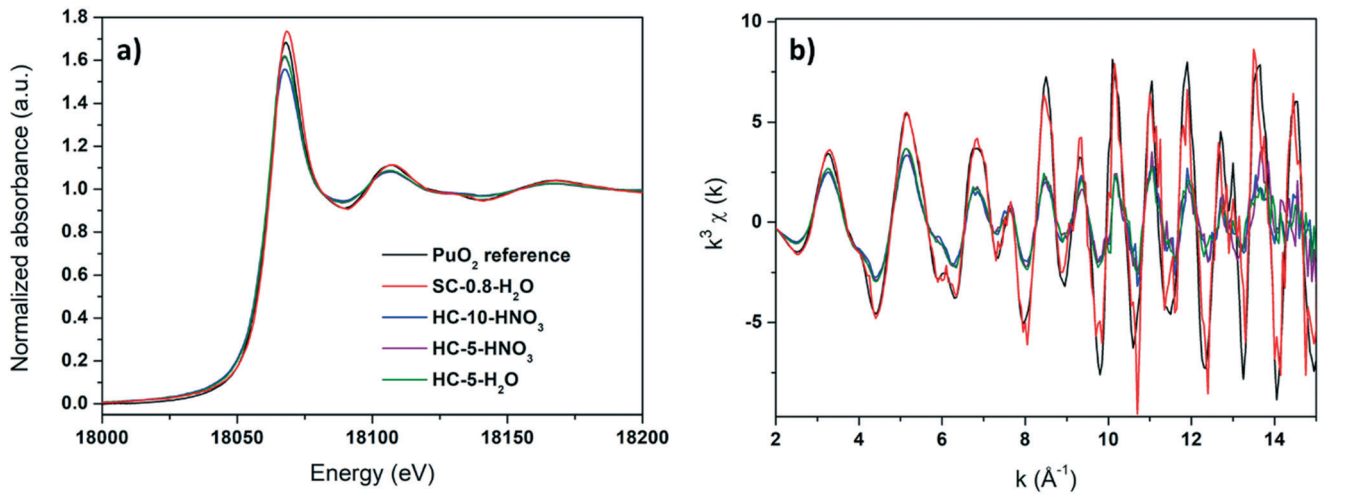


Fig. 5 a) Pu L_3 XANES and corresponding b) k^3-weighted experimental EXAFS spectra acquired on a selection of hydrolytic and sonolytic colloids (HC-10-HNO_3, HC-5-HNO_3, HC-5-H_2O and SC-0.8-H_2O). PuO_2 bulk powder is provided as a reference. The legend given in a) can be used for both figures.

Published on 29 June 2020. Downloaded by Los Alamos National Laboratory on 9/3/2025 11:23:41 PM.

in molecular Pu(IV) species. The similar XANES spectral shape observed for bulk PuO_2 and Pu intrinsic colloids was then attributed to a splitting of the 6d state crystal field.[50] These observations support the (+IV) oxidation states for the samples investigated in the current study. Slight energy shifts might be attributed to the potential presence of covalent Pu–O bonds expected for Pu(V) or Pu(VI) species (*trans* di-oxo bonds) and the observation of an "yl" shoulder at *ca.* 18 086 eV, a feature that is not observed for these samples, or at least too low to be noticed (see Fig. S11, ESI†).[50,52] Nanoparticle surface moieties (OH, H_2O, *etc.*) or structural defects such as O vacancies could also participate in XANES spectra variations. Slight WL variations have also been attributed to different aging and/or ripening processes for intrinsic Pu(IV) colloids.[53] The very small differences observed in Fig. 5a are not significant enough to be interpreted; the use of high resolution XANES techniques such as HERFD (high energy resolution fluorescence detection) as well as M edge measurements might provide further information.[50,54–56] Nevertheless, the used experimental conditions and the thorough inspection of our spectra at this stage suggest the very strong predominance of the (+IV) oxidation state for plutonium in the colloid samples (the exclusive presence of Pu(IV) cannot be affirmed from sole Pu L_{III} edge XANES spectra).

Fig. 5b provides the experimental k^3-weighted EXAFS functions that can be decomposed into low frequency oscillations in the 2–10 $Å^{-1}$ range and high frequency oscillations from 10 to 15 $Å^{-1}$. The overall shape of the spectra is similar for all of the samples. Nevertheless, the hydrolytic colloid samples can be distinguished from the sonolytic colloid with lower amplitude oscillations in both frequency ranges. The corresponding Fourier transforms (FT) obtained in the 2.5 $Å^{-1} < k < 15$ $Å^{-1}$ range gathered in Fig. 6 provide a pseudo-radial distribution function describing the coordination sphere of the absorbing Pu atoms (uncorrected for phase shift). These spectra show two main peaks at R–φ = *ca.* 1.84 and 3.68 Å in agreement with the k^3-weighted FT spectra of PuO_2 used as a reference, but also with previous reports dealing with intrinsic Pu(IV) colloids and PuO_2 samples.[22,51,57–60] This observation indicates that Pu intrinsic colloids exhibit some similarities with the structure of PuO_2 which crystallizes in the face centered cubic system. The position of the two peaks in bulk PuO_2 originates from the coordination of Pu(IV) with O and Pu atoms at *ca.* 2.33 Å and 3.81 Å, respectively.[61]

In comparison to PuO_2, two distinctive features can be observed for both hydrolytic and sonolytic colloid samples in Fig. 6. They indeed show (i) a reduced oscillation amplitude for both coordination shells, and (ii) a strong asymmetry and distortion of the Pu–O coordination sphere. Both effects are found significantly strengthened for the hydrolytic colloid samples in comparison to the sonolytic colloid whose spectrum appears intermediate between the hydrolytic ones and the PuO_2 reference. This observation shows a trend which agrees with the determined particle sizes probed by SAXS in

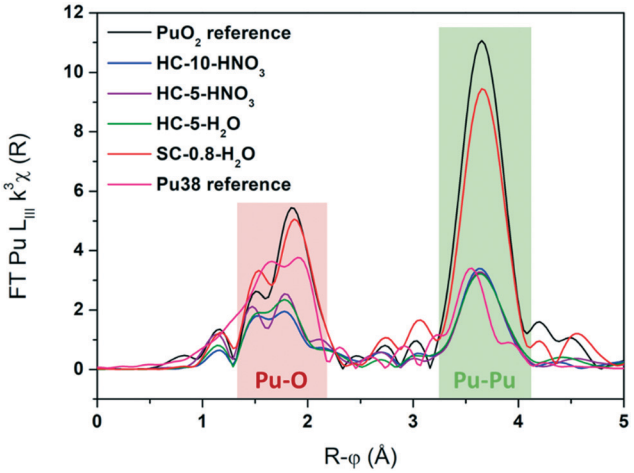


Fig. 6 Fourier transforms (FT) of the k^3-weighted 2.5–15 $Å^{-1}$ interval for a selection of hydrolytic and sonolytic Pu(IV) intrinsic colloids (HC-10-HNO_3, HC-5-HNO_3, HC-5-H_2O and SC-0.8-H_2O). Additional FT of the bulk PuO_2 and simulated Pu38 cluster are provided as references. The small peak standing at R–φ = 1.6 Å results from the μ_0 spline function subtraction when applied to $k_{max} > 11$ $Å^{-1}$. This treatment generates or suppresses very low frequency noise without any physical meaning for Pu–O distances.

the first part of the manuscript. It was previously suggested that the EXAFS amplitude reduction results from a strong local disorder in the bulk Pu atoms (decrease of crystallinity and increase of the DWF) and/or by a nanoparticle surface effect attributed to the increasing proportion of plutonium atoms standing at the particle surface in comparison to the bulk when decreasing in size (S/V atomic ratio).[15,22,36,51,53] The more specific distortion of the Pu–O coordination sphere has been suggested to result from a splitting of the Pu–O distances in the Pu oxide local structure. Several hypotheses have been discussed to explain the nature of these bonds including the presence of Pu–OH, Pu–O and Pu–H_2O distances, O defects or also the presence of short Pu=O oxo bonds found in Pu(V) or Pu(VI) moieties.[15,50,53,58,59,62] The two above hypotheses (bulk disorder and enhanced surface atom contribution) result in similar effects on the EXAFS spectra and are hence difficult to distinguish.

The aforementioned spectra variations are obviously related to a nanoscale effect and we emphasize that EXAFS interpretation becomes therefore challenging.[63] Particularly, these atomic scale variations constrain the data interpretation and analyses to a careful step by step process in which the outcome of any fit model must be considered with caution and self-criticism. Moreover, the double-electron excitation signal observed in the Pu L_{III} edge is likely to complicate the data treatment.[64] Performing fits of quality for such samples which exhibit PuO_2-like structures has been proved to be tricky and generally result from a compromise between the number of subshells used to reproduce the Pu–O coordination sphere and their corresponding Debye–Waller factor (DWF). Such assertions explain and reinforce our strategy involving the consideration of comparable samples exhibiting different

 This journal is © The Royal Society of Chemistry 2020

Published on 29 June 2020. Downloaded by Los Alamos National Laboratory on 9/3/2025 11:23:41 PM.

specific sizes and morphologies. In a previous study, we reproduced with good agreement the experimental EXAFS spectra of sonolytic and hydrolytic colloids using a constrained three O-shell model with Pu–O_{short} (for μ_1-Pu–OH or μ_3-Pu–O), Pu–O_{medium} (for μ_4-O from the PuO_2 ideal structure) and Pu–O_{long} (for surface-adsorbed H_2O molecules) distances. A good correlation was highlighted between the size of the colloids and the Pu–O_{short} coordination numbers suggested to hypothetical Pu–OH and μ_3-Pu–O moieties possibly standing at the surface of the nanoparticles.

We recently proposed an alternative fitting approach that allowed us to compare a selection of nanoscale AnO_2 oxide powders (An = Pu and Th).[36] Similarly, the FT EXAFS spectra acquired for these samples were found to agree with AnO_2 EXAFS spectra with differences in shell peak intensities and the observation of a distortion and asymmetry of the first An–O shell gradually increasing with the shrinking nanoparticles (or crystallites) comprising the samples. We used a single An–O scattering path to fit a Fourier filtered An–O sphere and determine the corresponding DWF, which is the only floating parameter in this approach but allows the local disorder around the absorbing atom to be measured. The results revealed a strong dependency between the as-obtained DWF parameters and the size of the nanoparticles (and/or crystallites) comprising the AnO_2 powder samples. Of particular interest was the similar behaviour evidenced between analogous ThO_2 and PuO_2 samples for which the DWF was found to consistently increase as a function of the decreasing crystallite size. Such a trend allowed the distortion of the An–O shell to be attributed to a nanoparticle effect and the contribution of high-valence Pu atoms in the measured PuO_2 samples to be excluded since the Th oxidation state is only (+IV) under these conditions. This last approach was considered in the current work and compared to fits obtained in a larger k range in order to discuss the results with regard to SAXS measurements and corresponding geometrical models. The extracted structural parameters, using the PuO_2-based fitting procedure described above and in the experimental section, are gathered in Table 4 (FT best fits and scattering paths provided in Fig. S12 and S13, ESI†). Furthermore, considering the small size of the particles (*ca.* 1 nm radius), we found it appropriate to compare our spectra with the crystallographic model of the Pu38 cluster published by Soderholm *et al.* (see description in the Experimental section and FT in Fig. 6).[12]

A progressive increase of the coordination numbers (CN) determined for the Pu–Pu shell can be observed between the different intrinsic colloid samples: the hydrolytic colloids range from 5.0(1.7) to 5.7(1.3) whereas the sonolytic colloid reaches 8.6(1.8) with Pu–Pu distances ranging between 3.80(1) and 3.82(1) Å. These CN values are framed by the values determined for PuO_2 (CN = 10.5(1.9)) and Pu38 (CN = 4.4(1.4)) references and confirm the highlighted trend correlating the DWF parameter and the size of the nanoparticle comprising the samples. Nevertheless, the DWF parameter determined using this procedure seems to underestimate the Pu–Pu coordination numbers. The theoretical Pu–Pu coordination number calculated from the crystallographic structure of the Pu38 cluster is 7.58 with a Pu–Pu interatomic distance ranging from 3.53 Å to 3.92 Å, whereas the fit results in only 4.4 Pu–Pu interactions at 3.80 Å. A similar comment can be raised with regard to the value obtained for the PuO_2 reference which can be assessed to be slightly lower than the theoretical one (CN_{Pu-Pu} = 10.5(1.9) instead of 12).[6,61] This Pu–Pu distance spreading could result from structural distortion in the Pu–O–Pu network as noticed in the Pu38 cluster[12] or suggested by Walther *et al.*[53] Also, a nanoparticle surface effect can be suggested as emphasized with nanoscale PuO_2 powders, recently.[36] In both cases, one could expect that the DWF must account for the Pu–Pu distance distribution resulting in more accurate CN obtained from a single scattering path. This approximation becomes wrong here since the Pu–Pu distance distribution becomes too large to be absorbed by the DWF parameter.

For the Pu–O shell, the determined DWF is the only floating parameter. The difference in the results provided in Table 4 for the two considered fit approaches confirms the influence of the spline function subtraction in the high k-range. It is indeed found that considering a too high k-range may involve an overestimation of the DWF parameter for the Pu–O shell that can misrepresent the distance distribution and corresponding CN. Nevertheless, a similar trend is observed for both approaches. Considering the 2.5–10 $Å^{-1}$ k-range, DWF equals

Table 4 EXAFS structural parameters calculated from k^3-weighted EXAFS spectra (CN: coordination number; R: interatomic distance, DWF: Debye–Waller factor). For the first Pu–O coordination sphere parameters, R_{Pu-O} = 2.33 Å and CN_{Pu-O} = 8, were fixed in accordance with the crystalline fcc PuO_2 structure. ΔE_0 = 4.8 eV, S_0^2 = 0.9. The standard deviations measured using IFEFFIT software are given in parentheses.[34] PuO_2 obtained by thermal conversion of Pu(IV) oxalate at 650 °C was used as a reference. Pu38 reference data were obtained from the crystallographic model published by Soderholm *et al.*[12]

Samples	DWF_{Pu-O}[a] (10^{-3} $Å^2$) k = 2.5–10 $Å^{-1}$	DWF_{Pu-O}[b] (10^{-3} $Å^2$) k = 2.5–15 $Å^{-1}$	CN_{Pu-Pu}[b]	R_{Pu-Pu}[b] (Å)	DWF_{Pu-Pu}[b] (10^{-3} $Å^2$) k = 2.5–15 $Å^{-1}$
Pu38 reference	14.9(1.2)		4.4(1.4)	3.80(1)	10.0(1.0)
HC-10-HNO_3	16.7(1.0)	15.2(1.0)	5.1(9)	3.81(1)	5.9(7)
HC-5-HNO_3	14.9(7)	13.5(7)	5.0(1.7)	3.80(1)	5.9(1.4)
HC-5-H_2O	15.0(8)	13.5(8)	5.7(1.3)	3.80(1)	6.7(8)
SC-0.8-H_2O	7.8(6)	6.8(1.0)	8.6(1.8)	3.82(1)	3.7(7)
PuO_2 reference	5.9(1.0)	5.9(9)	10.5(1.9)	3.81(1)	3.5(6)

[a] Values obtained using a FT acquired in a 2.5–10 $Å^{-1}$ truncated k-range. Fit was obtained with a single Pu–O path on the back FT performed on the as-filtered Pu–O sphere. [b] Values obtained in the 2.5–15 $Å^{-1}$ k-range. Fits were obtained with single Pu–O and Pu–Pu paths.

Published on 29 June 2020. Downloaded by Los Alamos National Laboratory on 9/3/2025 11:23:41 PM.

5.9×10^{-3} Å^2 for the PuO_2 reference, increases to 7.8×10^{-3} Å^2 for the sonolytic colloid, and reaches a maximum ranging from 14.9×10^{-3} Å^2 to 16.7×10^{-3} Å^2 for the hydrolytic colloid samples. This rising DWF parameter demonstrates an increasing disorder in the oxygen shell reflected by a splitting of the Pu–O distances which can be, once again, correlated to the nanoparticle shrinking that comprise the colloidal samples in agreement with SAXS data.[36] Using the single O-shell fit results in a DWF of 14.9×10^{-3} Å^2 for the small Pu38 model which is close but slightly lower than the one obtained for the HC-10-HNO_3 hydrolytic colloid. Interestingly, this observation is visually accompanied by a strong splitting and distortion of the Pu–O shell in the FT provided in Fig. 6. Obviously, this observation cannot be linked to the potential contribution of higher Pu oxidation states in the structure in agreement with the resolved structure of Pu38. Multiple Pu(IV)–O bonds in the Pu38 crystal structure rather explain the increase of the DWF such as the very short surface μ_3-O and μ_1-OH bonds at 2.1–2.2 Å as well as corner water molecules found at 2.5 Å. This indeed indicates that the same type of short surface bond is present at the colloid surface. Although being in the standard deviation, the absence of a significant difference between the determined DWF parameter for Pu38 and hydrolytic HC-10-HNO_3 can also be attributed to differences in surface roughness or thickness. A structural disorder in the core structure might also be proposed but appears less relevant considering previous XRD and HR-TEM results that demonstrated the crystalline nature of these colloid nanoparticles.

Several studies highlighted the more significant contribution of surface atoms in comparison to bulk when decreasing nanoparticle size (surface to volume ratio).[22,36,47] This phenomenon is particularly enhanced for nanoparticles measuring less than 10–20 nm in diameter. Geometric calculations allowed us to strengthen this statement by plotting the theoretical averaged Pu–Pu coordination number as a function of the nanoparticle radii (Fig. 7). The nanoparticle radius experimentally determined by SAXS and their Pu–Pu coordination numbers obtained from EXAFS simulations are superimposed in this figure to the geometrical calculations. The theoretical curves were drawn assuming spherical or disc nanoparticles in agreement with used SAXS models. The curves were plotted using a single Pu–Pu distance of 0.38 nm with coordination numbers of CN = 12 in the particle bulk and CN = 6 at the surface (only for the first Pu–Pu layer). A closer look at the Pu38 cluster indeed shows that the minimal CN for the Pu–Pu coordination sphere exhibited by surface Pu atoms is CN = 6. Therefore, the determined coordination numbers for nanoparticles exhibiting a spherical shape should not be lower than this value. Interestingly, the experimental points follow a trend similar to the geometrical model which is characterized by a fast increase of the average Pu–Pu CN value at the very beginning of the particle growth (Fig. 7). The elongated disc model used for the sonolytic colloid better explains the low coordination number for the Pu–Pu shell obtained by EXAFS for such big particles in

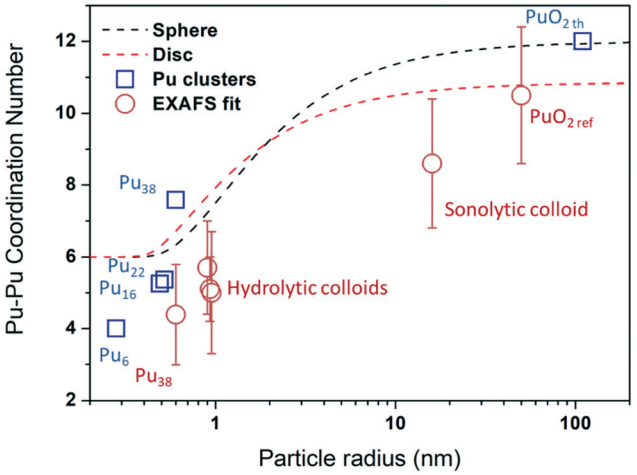


Fig. 7 Theoretical variation of the coordination number for the Pu–Pu coordination shell as a function of the radius for a sphere (dotted black line) or disc (dotted red line) model. The red circle plots (○) represent the experimental data (SAXS *vs.* EXAFS fit) and the blue squares (□) represent the theoretical CN for the Pu–Pu sphere calculated from the published crystallographic structures.

comparison to the spherical model. In addition, such elongated colloidal particles could in fact result from spherical particle aggregation (elongated PuO_2 nanoparticles are not observed in HR-TEM). However, an offset between both the experimental points and the geometrical model (for both spherical and disc shapes) is observed, thus strengthening our concerns about the fit accuracy to reproduce CN values for the Pu–Pu shell.

Several hypotheses can explain this discrepancy including some particle size polydispersity in addition to some core and surface structural differences. Several studies suggested that clusters made out of 38 actinide atoms are built from the olation and/or oxolation stacking of low nuclearity clusters involving 6, 16 or 22 atoms. Such observation has been highlighted for various actinides including uranium,[65] neptunium[66] and plutonium.[17] As shown in Fig. 7, Pu6, Pu16 and Pu22 clusters exhibit low coordination numbers measuring CN = 4, 5.23, and 5.36, respectively.[17,38,67] Thus, one might assume that the contribution of such species during the building of intrinsic colloids may contribute to lower coordination numbers for the Pu–Pu sphere. Hence, a higher amount of surface defects (*e.g.*, edges, corners, strains, steps…), surface groups (–OH functions, μ_3-oxo bonds, adsorbed water molecules…) and under-coordinated surface atoms can be expected for such nanoparticles.[15,22,36,46,51,53,63,68] These differences may also explain the slight WL XANES differences noted in Fig. 5a between our very similar samples. Several studies indeed demonstrated that XANES spectroscopy (and also EXAFS) may be significantly influenced by the more sensitive local geometry and electronic structure effects provided by nanoscale materials in comparison to bulk samples.[27,47,68,69]

 This journal is © The Royal Society of Chemistry 2020

Published on 29 June 2020. Downloaded by Los Alamos National Laboratory on 9/3/2025 11:23:41 PM.

Conclusions

To our knowledge, we performed the first combined synchrotron-based SAXS and XAS measurements of stable suspensions of intrinsic Pu(IV) colloids. This multi-scale approach allows the quasi-simultaneous probing of the size, morphology (*i.e.*, the shape) and local structure of the nanoparticles comprising the suspensions. Using this approach, the rigorous comparison of Pu(IV) intrinsic colloids prepared by hydrolysis and sonolysis demonstrates that the physico-chemical properties of the intrinsic Pu(IV) colloids are strongly influenced by the preparation method. The fast Pu(IV) hydrolysis in the presence of nitrate anions leads to 2.0(3) nm spherical nanoparticles characterized by reduced EXAFS spectra with an additional strong splitting of the Pu–O coordination shell. By contrast, sonolytic Pu(IV) intrinsic colloids prepared in pure water allow the observation of elongated bigger particles of *ca.* 5.7 nm thickness and more than 30 nm size (lamella/disk). The Pu–O shell distortion is less pronounced for this sample and the local structure appears intermediate between the hydrolytic colloid and bulk PuO_2 powder. Aggregation of nanoparticles in the case of this less stable suspension may explain this specific morphology.

More precisely, the highly debated Pu(IV) intrinsic colloids can be described as core–shell nanoparticles made out of a PuO_2 core surrounded by a disordered Pu–O shell solvated with nitrate counter-ions. The results obtained by both synchrotron SAXS and XAS approaches converge to the conclusion that the observed variations of the local structure for the intrinsic Pu colloids is strongly influenced by the nanoparticle surface when shrinking and highly unlikely results from the contribution of higher Pu oxidation states. The comparison with published data strongly suggests that the interfacial chemistry and nature contribute to the observed variations of the colloid local structure. These observations raise the question of the colloidal suspension stability (counter-ion concentration, colloid surface charge, radiolysis effect, *etc.*). Future investigations with different salt systems and more concentrated solutions should strengthen this approach and clarify the plutonium colloid shell nature. More generally, the multi-scale approach used in this study provides new insights about the local structure, size, morphology (*i.e.*, shape) and interfacial properties of intrinsic Pu(IV) colloids that could help in a better understanding of Pu migration mechanisms in the environment.

Author contributions

The manuscript was written through contributions of all authors who gave their approval for submission of the final version of the manuscript.

Conflicts of interest

There are no conflicts to declare.

Acknowledgements

We acknowledge the financial support of the Cross-Disciplinary Program on bottom up exploratory research program of CEA, the French Alternative Energies and Atomic Energy Commission. The authors gratefully acknowledge Jeremy Causse, Laëtitia Guerin, Myrtille Hunault, Emilie Russello, Bertrand Siboulet and Jackie Vermeulen for fruitful discussions and help in experiments. This work benefited from the use of the SasView application, originally developed under NSF award DMR-0520547. SasView contains code developed with funding from the European Union's Horizon 2020 research and innovation program under the SINE2020 project, grant agreement No. 654000.

References

1 A. B. Kersting, D. W. Efurd, D. L. Finnegan, D. J. Rokop, D. K. Smith and J. L. Thompson, Migration of plutonium in ground water at the Nevada Test Site, *Nature*, 1999, **397**, 56–59.

2 A. B. Kersting, Plutonium Transport in the Environment, *Inorg. Chem.*, 2013, **52**, 3533–3546.

3 C. Walther and M. A. Denecke, Actinide colloids and particles of environmental concern, *Chem. Rev.*, 2013, **113**, 995–1015.

4 Y. Li, L. Xu, P. Bai, G. Rong, D. Zhang, J. Diwu, W. Yan, Z. Chai and S. Wang, Emerging investigator series: significantly enhanced uptake of Eu^{3+} on a nanoporous zeolitic mineral in the presence of UO_2^{2+}: insights into the impact of cation–cation interaction on the geochemical behavior of lanthanides and actinides, *Environ. Sci.: Nano*, 2019, **6**, 736–746.

5 E. L. Tran, O. Klein-BenDavid, N. Teutsch and N. Weisbrod, Influence of Intrinsic Colloid Formation on Migration of Cerium through Fractured Carbonate Rock, *Environ. Sci. Technol.*, 2015, **49**, 13275–13282.

6 D. Clark, S. Hecker, G. Jarvinen and M. Neu, in *The Chemistry of the Actinide and Transactinide Elements*, ed. L. Morss, N. Edelstein and J. Fuger, Springer, Netherlands, 2011, ch. 7, pp. 813–1264, DOI: 10.1007/978-94-007-0211-0_7.

7 T. Kobayashi, T. Sasaki, I. Takagi and H. Moriyama, Effect of solid phase transformation on the solubility product of thorium hydrous oxide at 363 K, *J. Nucl. Sci. Technol.*, 2016, **53**, 1787–1793.

8 P. W. Schindler, in *Equilibrium Concepts in Natural Water Systems*, American Chemical Society, 1967, ch. 9, vol. 67, pp. 196–221.

9 A. E. Hixon and B. A. Powell, Observed Changes in the Mechanism and Rates of Pu(V) Reduction on Hematite As a Function of Total Plutonium Concentration, *Environ. Sci. Technol.*, 2014, **48**, 9255–9262.

10 B. A. Powell, Z. R. Dai, M. Zavarin, P. H. Zhao and A. B. Kersting, Stabilization of plutonium nano-colloids by epitaxial distortion on mineral surfaces, *Environ. Sci. Technol.*, 2011, **45**, 2698–2703.

Published on 29 June 2020. Downloaded by Los Alamos National Laboratory on 9/3/2025 11:23:41 PM.

11 K. Reed, A. Cormack, A. Kulkarni, M. Mayton, D. Sayle, F. Klaessig and B. Stadler, Exploring the properties and applications of nanoceria: is there still plenty of room at the bottom?, *Environ. Sci.: Nano*, 2014, **1**, 390–405.

12 L. Soderholm, P. M. Almond, S. Skanthakumar, R. E. Wilson and P. C. Burns, The structure of the Plutonium oxide nanocluster $Pu_{38}O_{56}Cl_{54}(H_2O)_{(8)}^{(14-)}$, *Angew. Chem., Int. Ed.*, 2008, **47**, 298–302.

13 D. A. Costanzo, R. E. Biggers and J. T. Bell, Plutonium polymerization.1. Spectrophotometric study of polymerization of plutonium(IV), *J. Inorg. Nucl. Chem.*, 1973, **35**, 609–622.

14 U. Kaplan, S. Amayri, J. Drebert, A. Rossberg, D. Grolimund and T. Reich, Geochemical Interactions of Plutonium with Opalinus Clay Studied by Spatially Resolved Synchrotron Radiation Techniques, *Environ. Sci. Technol.*, 2017, **51**, 7892–7902.

15 J. Rothe, C. Walther, M. A. Denecke and T. Fanghanel, XAFS and LIBD investigation of the formation and structure of colloidal Pu(IV) hydrolysis products, *Inorg. Chem.*, 2004, **43**, 4708–4718.

16 V. Neck and J. I. Kim, Solubility and hydrolysis of tetravalent actinides, *Radiochim. Acta*, 2001, **89**, 1–16.

17 G. E. Sigmon and A. E. Hixon, Extension of the Plutonium Oxide Nanocluster Family to Include {Pu-16} and {Pu-22}, *Chem. – Eur. J.*, 2019, **25**, 2463–2466.

18 T. W. Newton, D. E. Hobart and P. D. Palmer, The formation of Pu(IV) colloid by the alpha-reduction of Pu(V) or Pu(VI) in aqueous solutions, *Radiochim. Acta*, 1986, **39**, 139–147.

19 I. R. Triay, D. E. Hobart, A. J. Mitchell, T. W. Newton, M. A. Ott, P. D. Palmer, R. S. Rundberg and J. L. Thompson, Size determinations of plutonium colloids using autocorrelation photon spectroscopy, *Radiochim. Acta*, 1991, **52–53**, 127–131.

20 P. Thiyagarajan, H. Diamond, L. Soderholm, E. P. Horwitz, L. M. Toth and L. K. Felker, Plutonium(IV) polymers in aqueous and organic media, *Inorg. Chem.*, 1990, **29**, 1902–1907.

21 D. Rai and J. L. Swanson, Properties of plutonium(IV) polymer of environmental importance, *Nucl. Technol.*, 1981, **54**, 107–112.

22 E. Dalodiere, M. Virot, V. Morosini, T. Chave, T. Dumas, C. Hennig, T. Wiss, O. D. Blanco, D. K. Shuh, T. Tyliszcak, L. Venault, P. Moisy and S. I. Nikitenko, Insights into the sonochemical synthesis and properties of salt-free intrinsic plutonium colloids, *Sci. Rep.*, 2017, **7**, 43514, DOI: 10.1038/srep43514.

23 P. Zhao, M. Zavarin, Z. Dai and A. B. Kersting, *Pu Sorption, Desorption and Intrinsic Colloid Stability under Granitic Chemical Conditions*, United States: N. p., 2014. Web, Report LLNL-TR-659761, Lawrence Livermore National Lab. (LLNL), Livermore, CA (United States), 2014, DOI: 10.2172/1169859.

24 S. Mourdikoudis, R. M. Pallares and N. T. K. Thanh, Characterization techniques for nanoparticles: comparison and complementarity upon studying nanoparticle properties, *Nanoscale*, 2018, **10**, 12871–12934.

25 F. Tao and P. A. Crozier, Atomic-scale observations of catalyst structures under reaction conditions and during catalysis, *Chem. Rev.*, 2016, **116**, 3487–3539.

26 R. J. Batrice, J. N. Wacker and K. E. Knope, in *Experimental and Theoretical Approaches to Actinide Chemistry*, ed. J. K. Gibson and W. A. Jong, 2018, pp. 53–127, DOI: 10.1002/9781119115557.ch2.

27 A. Y. Romanchuk, T. V. Plakhova, A. V. Egorov, T. B. Egorova, P. V. Dorovatovskii, Y. V. Zubavichus, A. A. Shiryaev and S. N. Kalmykov, Redox-mediated formation of plutonium oxide nanoparticles, *Dalton Trans.*, 2018, **47**, 11239–11244.

28 X. Beaudoux, M. Virot, T. Chave, G. Leturcq, G. Jouan, L. Venault, P. Moisy and S. I. Nikitenko, Ultrasound-assisted reductive dissolution of CeO_2 and PuO_2 in the presence of Ti particles, *Dalton Trans.*, 2016, **45**, 8802–8815.

29 V. Morosini, T. Chave, M. Virot, P. Moisy and S. I. Nikitenko, Sonochemical water splitting in the presence of powdered metal oxides, *Ultrason. Sonochem.*, 2016, **29**, 512–516.

30 D. H. Everett, Manual of Symbols and Terminology for Physicochemical Quantities and Units, Appendix II: Definitions, Terminology and Symbols in Colloid and Surface Chemistry, *Pure Appl. Chem.*, 1972, **31**(4), 577, DOI: 10.1351/pac197231040577.

31 R. E. Wilson, S. Skanthakumar and L. Soderholm, Separation of Plutonium Oxide Nanoparticles and Colloids, *Angew. Chem., Int. Ed.*, 2011, **50**, 11234–11237.

32 B. Sitaud, P. L. Solari, S. Schlutig, I. Llorens and H. Hermange, Characterization of radioactive materials using the MARS beamline at the synchrotron SOLEIL, *J. Nucl. Mater.*, 2012, **425**, 238–243.

33 M. Doucet, J. H. Cho, G. Alina, J. Bakker, W. Bouwman, P. Butler, K. Campbell, M. Gonzales, R. Heenan, A. Jackson, P. Juhas, S. King, P. Kienzle, J. Krzywon, A. Markvardsen, T. Nielsen, L. O'Driscoll, W. Potrzebowski, R. Ferraz Leal, T. Richter, P. Rozycko, T. Snow and A. Washington, *SasView version 4.2 (Version 4.2.0)*, Zenodo, 2018, DOI: 10.5281/zenodo.1412041.

34 B. Ravel and M. Newville, ATHENA, ARTEMIS, HEPHAESTUS: data analysis for X-ray absorption spectroscopy using IFEFFIT, *J. Synchrotron Radiat.*, 2005, **12**, 537–541.

35 J. J. Rehr, J. J. Kas, M. P. Prange, A. P. Sorini, Y. Takimoto and F. Vila, Ab initio theory and calculations of X-ray spectra, *C. R. Phys.*, 2009, **10**, 548–559.

36 L. Bonato, M. Virot, E. Dalodière, T. Dumas, A. Mesbah, O. Dieste Blanco, T. Wiss, D. Prieur, A. Rossberg, L. Venault, P. Moisy and S. I. Nikitenko, Probing the local structure of nanoscaled actinide oxides: a comparison between PuO_2 and ThO_2 nanoparticles rules out PuO_{2+x} hypothesis, *Nanoscale Adv.*, 2020, **2**, 214–224, DOI: 10.1039/C9NA00662A.

37 K. Takao, S. Takao, A. C. Scheinost, G. Bernhard and C. Hennig, Formation of Soluble Hexanuclear Neptunium(IV) Nanoclusters in Aqueous Solution: Growth Termination of Actinide(IV) Hydrous Oxides by Carboxylates, *Inorg. Chem.*, 2012, **51**, 1336–1344.

38 C. Tamain, T. Dumas, D. Guillaumont, C. Hennig and P. Guilbaud, First Evidence of a Water-Soluble Plutonium(IV) Hexanuclear Cluster, *Eur. J. Inorg. Chem.*, 2016, 3536–3540, DOI: 10.1002/ejic.201600656.

39 C. Walther, H. R. Cho, C. M. Marquardt, V. Neck, A. Seibert, J. I. Yun and T. Fanghanel, Hydrolysis of plutonium(IV) in

 This journal is © The Royal Society of Chemistry 2020

Published on 29 June 2020. Downloaded by Los Alamos National Laboratory on 9/3/2025 11:23:41 PM.

acidic solutions: no effect of hydrolysis on absorption-spectra of mononuclear hydroxide complexes, *Radiochim. Acta*, 2007, **95**, 7–16.

40 D. W. Ockenden and G. A. Welch, The preparation and properties of some plutonium compounds.5. Colloidal quadrivalent plutonium, *J. Chem. Soc.*, 1956, 3358–3363, DOI: 10.1039/jr9560003358.

41 D. Cohen, The absorption spectra of plutonium ions in perchloric acid solutions, *J. Inorg. Nucl. Chem.*, 1961, **18**, 211–218.

42 L. Boldon, F. Laliberte and L. Liu, Review of the fundamental theories behind small angle X-ray scattering, molecular dynamics simulations, and relevant integrated application, *Nano Rev.*, 2015, **6**, 25661–25661.

43 O. Glatter and O. Kratky, *Small angle x-ray scattering*, Academic Press, London, New York, 1982.

44 T. Li, A. J. Senesi and B. Lee, Small Angle X-ray Scattering for Nanoparticle Research, *Chem. Rev.*, 2016, **116**, 11128–11180.

45 F. Nallet, *Introduction à la diffusion aux petits angles*, La Gerande Motte, 2009.

46 T. V. Plakhova, A. Y. Romanchuk, S. M. Butorin, A. D. Konyukhova, A. V. Egorov, A. A. Shiryaev, A. E. Baranchikov, P. V. Dorovatovskii, T. Huthwelker, E. Gerber, S. Bauters, M. M. Sozarukova, A. C. Scheinost, V. K. Ivanov, S. N. Kalmykov and K. O. Kvashnina, Towards the surface hydroxyl species in CeO_2 nanoparticles, *Nanoscale*, 2019, **11**, 18142–18149, DOI: 10.1039/c9nr06032d.

47 L. Amidani, T. V. Plakhova, A. Y. Romanchuk, E. Gerber, S. Weiss, A. Efimenko, C. J. Sahle, S. M. Butorin, S. N. Kalmykov and K. O. Kvashnina, Understanding the size effects on the electronic structure of ThO_2 nanoparticles, *Phys. Chem. Chem. Phys.*, 2019, **21**, 10635–10643.

48 A. I. Abdel-Fattah, D. X. Zhou, H. Boukhalfa, S. Tarimala, S. D. Ware and A. A. Keller, Dispersion stability and electrokinetic properties of intrinsic plutonium colloids: implications for subsurface transport, *Environ. Sci. Technol.*, 2013, **47**, 5626–5634.

49 H. K. Roobottom, H. D. B. Jenkins, J. Passmore and L. Glasser, Thermochemical radii of complex ions, *J. Chem. Educ.*, 1999, **76**, 1570–1573.

50 T. Vitova, I. Pidchenko, D. Fellhauer, T. Pruessmann, S. Bahl, K. Dardenne, T. Yokosawa, B. Schimmelpfennig, M. Altmaier, M. Denecke, J. Rothe and H. Geckeis, Exploring the electronic structure and speciation of aqueous and colloidal Pu with high energy resolution XANES and computations, *Chem. Commun.*, 2018, **54**, 12824–12827.

51 D. Hudry, C. Apostolidis, O. Walter, A. Janssen, D. Manara, J. C. Griveau, E. Colineau, T. Vitova, T. Prussmann, D. Wang, C. Kubel and D. Meyer, Ultra-small plutonium oxide nanocrystals: an innovative material in plutonium science, *Chem. – Eur. J.*, 2014, **20**, 10431–10438.

52 E. Dalodière, M. Virot, T. Dumas, D. Guillaumont, M.-C. Illy, C. Berthon, L. Guerin, A. Rossberg, L. Venault, P. Moisy and S. I. Nikitenko, Structural and magnetic susceptibility characterization of Pu(v) aqua ion using sonochemistry as a facile synthesis method, *Inorg. Chem. Front.*, 2018, **5**, 100–111.

53 C. Walther, J. Rothe, B. Brendebach, M. Fuss, M. Altmaier, C. M. Marquardt, S. Büchner, H.-R. Cho, J.-I. Yun and A. Seibert, New insights in the formation processes of Pu(IV) colloids, *Radiochim. Acta*, 2009, **97**, 199–207, DOI: 10.1524/ract.2009.1595.

54 K. O. Kvashnina, S. M. Butorin, P. Martin and P. Glatzel, Chemical State of Complex Uranium Oxides, *Phys. Rev. Lett.*, 2013, **111**, 253002.

55 K. O. Kvashnina, H. C. Walker, N. Magnani, G. H. Lander and R. Caciuffo, Resonant x-ray spectroscopy of uranium intermetallics at the M-4,M-5 edges of uranium, *Phys. Rev. B*, 2017, **95**, 245103, DOI: 10.1103/PhysRevB.95.245103.

56 M. Hunault, G. Lelong, L. Cormier, L. Galoisy, P. L. Solari and G. Calas, Speciation Change of Uranyl in Lithium Borate Glasses, *Inorg. Chem.*, 2019, **58**, 6858–6865.

57 C. Ekberg, K. Larsson, G. Skarnemark, A. Odegaard-Jensen and I. Persson, The structure of plutonium(IV) oxide as hydrolysed clusters in aqueous suspensions, *Dalton Trans.*, 2013, **42**, 2035–2040.

58 S. D. Conradson, B. D. Begg, D. L. Clark, C. Den Auwer, F. J. Espinosa-Faller, P. L. Gordon, N. J. Hess, R. Hess, D. W. Keogh, L. A. Morales, M. P. Neu, W. Runde, C. D. Tait, D. K. Veirs and P. M. Villella, Speciation and unusual reactivity in PuO_{2+x}, *Inorg. Chem.*, 2003, **42**, 3715–3717.

59 S. D. Conradson, B. D. Begg, D. L. Clark, C. den Auwer, M. Ding, P. K. Dorhout, F. J. Espinosa-Faller, P. L. Gordon, R. G. Haire, N. J. Hess, R. F. Hess, D. W. Keogh, G. H. Lander, D. Manara, L. A. Morales, M. P. Neu, P. Paviet-Hartmann, J. Rebizant, V. V. Rondinella, W. Runde, C. D. Tait, D. K. Veirs, P. M. Villella and F. Wastin, Charge distribution and local structure and speciation in the UO_{2+x} and PuO_{2+x} binary oxides for $x <= 0.25$, *J. Solid State Chem.*, 2005, **178**, 521–535.

60 P. Martin, S. Grandjean, M. Ripert, M. Freyss, P. Blanc and T. Petit, Oxidation of plutonium dioxide: an X-ray absorption spectroscopy study, *J. Nucl. Mater.*, 2003, **320**, 138–141.

61 P. Martin, S. Grandjean, M. Ripert, M. Freyss, P. Blanc and T. Petit, Oxidation of plutonium dioxide: an X-ray absorption spectroscopy study, *J. Nucl. Mater.*, 2003, **320**, 138–141.

62 M. Altmaier, X. Gaona and T. Fanghänel, Recent Advances in Aqueous Actinide Chemistry and Thermodynamics, *Chem. Rev.*, 2013, **113**, 901–943.

63 A. Kuzmin and J. Chaboy, EXAFS and XANES analysis of oxides at the nanoscale, *IUCrJ*, 2014, **1**, 571–589.

64 C. Hennig, Evidence for double-electron excitations in the L-3-edge x-ray absorption spectra of actinides, *Phys. Rev. B: Condens. Matter Mater. Phys.*, 2007, **75**, 035120, DOI: 10.1103/PhysRevB.75.035120.

65 L. Chatelain, R. Faizova, F. Fadaei-Tirani, J. Pecaut and M. Mazzanti, Structural Snapshots of Cluster Growth from {U-6} to {U-38} During the Hydrolysis of UCl4, *Angew. Chem., Int. Ed.*, 2019, **58**, 3021–3026.

66 N. P. Martin, C. Volkringer, P. Roussel, J. Marz, C. Hennig, T. Loiseau and A. Ikeda-Ohno, {Np-38} clusters: the missing link in the largest poly-oxo cluster series of tetravalent actinides, *Chem. Commun.*, 2018, **54**, 10060–10063.

67 K. E. Knope and L. Soderholm, Plutonium(IV) Cluster with a Hexanuclear $Pu_6(OH)(4)O_4^{(12+)}$ Core, *Inorg. Chem.*, 2013, **52**, 6770–6772.
68 A. I. Frenkel, C. W. Hills and R. G. Nuzzo, A view from the inside: Complexity in the atomic scale ordering of supported metal nanoparticles, *J. Phys. Chem. B*, 2001, **105**, 12689–12703.
69 A. I. Frenkel, C. W. Hills and R. G. Nuzzo, A View from the Inside: Complexity in the Atomic Scale Ordering of Supported Metal Nanoparticles, *J. Phys. Chem. B*, 2001, **105**, 12689–12703.

Published on 29 June 2020. Downloaded by Los Alamos National Laboratory on 9/3/2025 11:23:41 PM.

 This journal is © The Royal Society of Chemistry 2020